Trajectory-based Non-adiabatic Simulations of the Polariton Relaxation Dynamics

Deping Hu[†],[1, a)] Benjamin X. K. Chng[†],[2] Wenxiang Ying,[3] and Pengfei Huo[3, 4, b)]
[1)] *Center for Advanced Materials Research, Beijing Normal University, Zhuhai 519087, China*
[2)] *Department of Physics and Astronomy, University of Rochester, Rochester, NY 14627, U.S.A.*
[3)] *Department of Chemistry, University of Rochester, 120 Trustee Road, Rochester, NY 14627, U.S.A.*
[4)] *The Institute of Optics, Hajim School of Engineering, University of Rochester, Rochester, New York, 14627, U.S.A.*

We benchmark the accuracy of various trajectory-based non-adiabatic methods in simulating the polariton relaxation dynamics under the collective coupling regime. The Holstein-Tavis-Cummings (HTC) Hamiltonian is used to describe the hybrid light-matter system of N molecules coupled to a single cavity mode. We apply various recently developed trajectory-based methods to simulate the population relaxation dynamics by initially exciting the upper polariton state, and benchmark the results against populations computed from exact quantum dynamical propagation using the hierarchical equations of motion (HEOM) approach. In these benchmarks, we have systematically varied the number of molecules N, light-matter detunings, and the light-matter coupling strengths. Our results demonstrate that the symmetrical quasi-classical method with γ correction (γ-SQC) and spin-mapping linearized semi-classical (spin-LSC) approaches yield more accurate polariton population dynamics than traditional mixed quantum-classical (MQC) methods such as the Ehrenfest and surface hopping techniques.

I. INTRODUCTION

Molecular cavity quantum electrodynamics (QED) systems, which contain strongly interacting molecules with quantized cavity photonic modes, are emerging quantum systems that exhibit new phenomena in chemistry and physics.[1–7] Previous theoretical studies have shown that these hybrid light-matter states, so-called polaritons,[2,3,8–11], can modify chemical reactions via light-matter coupling.[2,3,9,12–14] In addition, recent experiments have shown that molecular polaritons have drastically different transport properties compared to their bare excitonic components, paving the way for efficient and scalable optoelectronic devices based on polaritons[15–20]. The light-matter hybridization also partially reduces the influence of phonons on the polariton, because the photon component does not couple to the phonon. This leads to the polaron decoupling effect[21,22] and the well-known absorption lineshape narrowing.[23,24]

In particular, coupling N molecular exciton states with a quantized cavity mode produces two polariton states, commonly referred to as the upper polariton (UP) and lower polariton (LP) states, each containing light and matter excitation characters. There are $N-1$ remaining dark exciton states that do not mix with photonic states or have a significant transition dipole from the ground state, and are thus optically dark. Upon photoexcitation to UP, the system will quickly relax to the dark states and slowly transition to the lower polaritons.[25,26] Polariton relaxation dynamics play a crucial role in understanding the polariton photoluminescence spectra,[26–29] understanding the relative lifetime of the polariton and dark states,[25,27] interpret the sub-average behavior of motional narrowing,[30] and the transition rates between the polaritons and dark states,[25] as well as the corresponding decoherence process.[31]

To study polariton relaxation dynamics, one often uses the Holstein-Tavis-Cummings (HTC) Hamiltonian[5,6,21,26,32,33] to model the interplay between the exciton, photon, and phonon degrees of freedom (DOF). The HTC model couples many molecules, which are described as two-level systems, to both a cavity photon mode and phonon modes that are added phenomenologically to the molecules. In the strong-coupling regime, it has been shown that the HTC Hamiltonian captures the underlying physics of the cavity-QED systems[6,7,26,34–38], such as the polariton's relaxation dynamics[6,25,26,37] and the polaron decoupling effect between excitons and their corresponding phonon modes[23,39].

A popular approach to simulate the non-adiabatic dynamics of systems with coupled electronic-nuclear degree of freedom is the mixed quantum-classical (MQC) methods[40–43], which has been widely used to model polariton relaxation dynamics.[5,6,33] Two commonly used MQC methods are the mean-field Ehrenfest method (MFE)[44] and the surface hopping method.[45,46] These methods treat the electronic DOFs quantum mechanically while propagating the nuclear DOFs classically (while often sampling the initial condition through quantum Wigner distributions). To simulate the dynamics of molecular polaritons, one extends the MQC approaches to treat both the electronic and photonic DOFs quantum mechanically while propagating the nuclear DOFs classically[4–7,47–53]. However, the mixed quantum-classical approximations built into these methods have

[a)] Electronic mail: depinghu@bnu.edu.cn
[b)] Electronic mail: pengfei.huo@rochester.edu

been known to produce unphysical results, such as the breakdown of detailed balance (that is, the long-term populations) for the MFE method[54] and the introduction of artificial electronic coherence or incorrect chemical kinetics for the surface hopping method[55].

To address the shortcomings of the MQC approaches above, other non-adiabatic dynamics methods have been developed in the diabatic representation, several of which are based on mapping formalism.[56,57] For example, methods such as the partially linearized density matrix (PLDM) method[58,59], symmetrical quasi-classical (SQC) method[60,61], and the quantum-classical Liouville equation (QCLE) method[62,63] are developed based on the Meyer-Miller-Stock-Thoss (MMST) mapping formalism[56,64,65]. Further, methods such as the spin-mapped linearized semi-classical (spin-LSC)[66–68] and the spin-mapped partially linearized density matrix (spin-PLDM) method[69,70] are derived from the recently developed generalized spin-mapping formalism, which uses the generalized spin-mapping relations to describe the electronic DOF[67] while using a linearized approximation for the nuclear DOF[71,72]. These methods have shown significant improvements in numerical results over existing MQC approaches, such as in characterizing the population dynamics of spin-boson models[66] exciton dynamics in light-harvesting complexes,[67] ab initio on-the-fly simulations,[73–76] as well as exciton-polariton quantum dynamics[52] and vibrational polariton quantum dynamics.[43] Based on these previous results, these non-adiabatic dynamical methods based on mapping formalism should also outperform MQC methods in simulating the polariton relaxation dynamics, although there have been limited investigations into the efficacy of these methods for polaritonic systems.[23,26,27,43,77,78]

In this paper, we use the Ehrenfest method, global flux surface-hopping (GFSH) method[79], SQC method with corrected zero-point energy (γ-SQC)[80] and spin-LSC method,[67,81] to simulate the population dynamics of a system that is initially excited into the upper polariton state. These methods are benchmarked with the numerically exact hierarchical equations of motion (HEOM) approach[82–84]. Numerical results are presented for HTC models with different physical parameters, such as the number of molecules that are coupled to the cavity mode, the single-molecule coupling strength, the light-matter detunings, and various parameters for the phonon bath. Our results provide valuable information on the accuracy of the commonly used MQC methods and the recently developed mapping approaches for simulating polariton relaxation dynamics in the HTC model.

II. THEORY AND METHODS

A. The Holstein-Tavis-Cummings QED Hamiltonian

We use the Holstein-Tavis-Cummings (HTC) Hamiltonian[1,22,26,85,86] to model the polariton dynamics in the collective coupling regime. The total Hamiltonian can be separated into a component describing the system term $\hat{H}_{\mathrm{S}}$, a component describing the bath term $\hat{h}_{\mathrm{B}}$, and a system-bath interaction term $\hat{H}_{\mathrm{SB}}$. This separation of terms is expressed as

$$\hat{H}_{\mathrm{HTC}} = \hat{H}_{\mathrm{S}} + \hat{h}_{\mathrm{B}} + \hat{H}_{\mathrm{SB}}. \tag{1}$$

In the remainder of the paper, we use units $\hbar = 1$ for convenience.

The system term $\hat{H}_{\mathrm{S}}$ consists of the excitonic DOF of the molecules and the photonic DOF of the cavity and is further expressed as[31,87]

$$\hat{H}_{\mathrm{S}} = \hat{H}_{\mathrm{M}} + \hat{H}_{\mathrm{cav}} + \hat{H}_{\mathrm{LM}}, \tag{2}$$

where $\hat{H}_{\mathrm{M}}$ describes the matter contribution due to the excitonic DOF, $\hat{H}_{\mathrm{cav}}$ describes the cavity contribution, and $\hat{H}_{\mathrm{LM}}$ is the light-matter interaction term. The matter contribution $\hat{H}_{\mathrm{M}}$ to the Hamiltonian describes N identical and non-interacting molecules. In this description, each molecule is modeled as an effective two-level system that represents the molecule's ground and excited states. The resulting Hamiltonian is written as

$$\hat{H}_{\mathrm{M}} = (\omega_a + \lambda) \sum_{n=1}^{N} \hat{\sigma}_n^{\dagger} \hat{\sigma}_n, \tag{3}$$

where $\hat{\sigma}_n^{\dagger} = |e_n\rangle\langle g_n|$ and $\hat{\sigma}_n = |g_n\rangle\langle e_n|$ creates and annilates an excitation on the n_{th} molecule, respectively, with $|g_n\rangle$ and $|e_n\rangle$ as the ground and excited states for molecule n, and ω_a is the excitation energy between the molecule's ground and excited state. The corresponding reorganization energy λ is due to exciton-phonon coupling, which is described in the system-bath interaction $\hat{H}_{\mathrm{SB}}$ (see Eq. 7).

The quantized radiation mode of the cavity is expressed as

$$\hat{H}_{\mathrm{cav}} = \omega_{\mathrm{c}}(\hat{a}^{\dagger}\hat{a} + \frac{1}{2}), \tag{4}$$

where ω_{c} is the photon frequency of the cavity mode, and $\hat{a}^{\dagger}$ and $\hat{a}$ are the creation and annihilation operators for a photon in the cavity mode. Here, we consider only a single cavity mode interacting with the molecules.

For the light-matter interaction term $\hat{H}_{\mathrm{LM}}$, we assume the long-wavelength approximation, that is, each molecule is coupled to the quantized radiation field with the same light-matter coupling strength g_{c}. Assuming the rotating wave approximation, $\hat{H}_{\mathrm{LM}}$ is expressed as

$$\hat{H}_{\mathrm{LM}} = g_{\mathrm{c}} \sum_{n=1}^{N_a} \left(\hat{a}^{\dagger}\hat{\sigma}_n^{-} + \hat{a}\hat{\sigma}_n^{+}\right) \tag{5}$$

The bath Hamiltonian $\hat{h}_{\mathrm{B}}$ in Eq. 1 describes the nuclear DOF, which we assume is a phonon environment

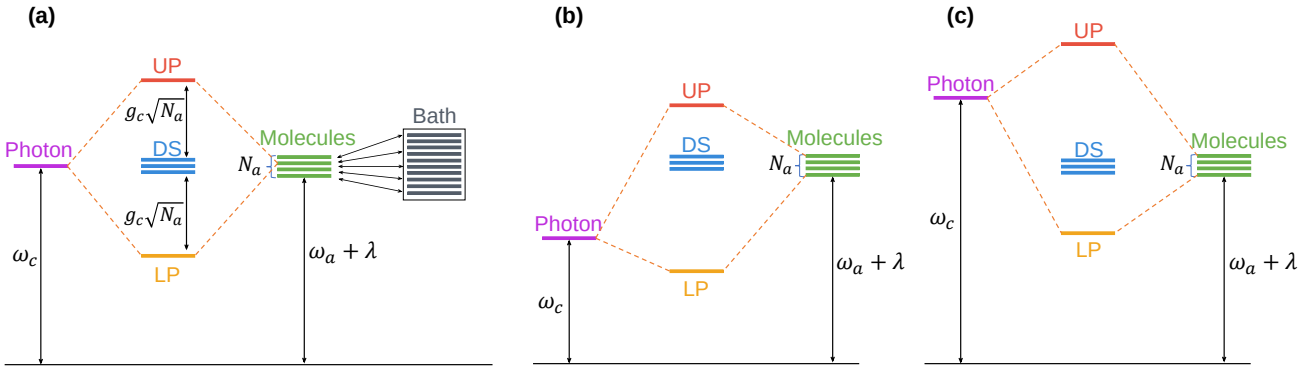

Figure 1. The energy level diagrams of polariton states that are derived from the HTC Hamiltonian through hybridization of light and matter states. We show the relative positions of the dark states with respect to the upper and lower polaritons for three cases: a) $\omega_c = \omega_a + \lambda$ (zero detuning or resonance), b) $\omega_c < \omega_a + \lambda$ (negative detuning) c) $\omega_c > \omega_a + \lambda$ (positive detuning).

that consists of a set of identical, non-interacting harmonic oscillators:

$$\hat{h}_{\mathrm{B}} = \sum_{n=1}^{N} \sum_{k} \omega_k (\hat{\nu}_{k,n}^{\dagger} \hat{\nu}_{k,n} + \frac{1}{2}), \tag{6}$$

where ω_k are the phonon frequencies, and $\hat{\nu}_{k,n}^{\dagger}$ and $\hat{\nu}_{k,n}$ are the k_{th} phonon mode's creation and annihilation operators for the n_{th} molecule that satisfy the bosonic commutation relations. The last term $\hat{H}_{\mathrm{SB}}$ in Eq. 1. characterizes the system-bath interaction, which we assume takes the linear form,

$$\hat{H}_{\mathrm{SB}} = \sum_{n} \hat{\sigma}_n^{+} \hat{\sigma}_n^{-} \sum_{k} c_k \left(\hat{\nu}_{k,n}^{\dagger} + \hat{\nu}_{k,n} \right), \tag{7}$$

where c_k denotes the coupling strength between the n_{th} molecule and the k_{th} phonon mode of its associated bath. To describe the interactions between the system and bath, we use the spectral density function[88,89]

$$J(\omega) = \pi \sum_{k} c_k^2 \delta(\omega - \omega_k). \tag{8}$$

We use a Drude-Lorentz form for the spectral density in our investigations,

$$J(\omega) = \frac{2\lambda\omega_\nu\omega}{\omega_\nu^2 + \omega^2} \tag{9}$$

where ω_ν is the bath characteristic frequency, and the reorganization energy λ can be reformulated in terms of the coupling strength and the phonon frequencies as

$$\lambda = \frac{1}{\pi} \int_0^{+\infty} d\omega \, \frac{J(\omega)}{\omega} = \sum_{k} \frac{c_k^2}{\omega_k}. \tag{10}$$

Cavity loss is not considered in this work becasue our aim is to benchmark the influence of phonons on polariton relaxation dynamics. The influence of cavity loss can be easily modeled with Lindblad dynamics,[53,90] or through stochastic Lindblad approaches[23,90]

B. Polariton States

We analyze $\hat{H}_{\mathrm{S}}$ in the single excitation subspace. The diabatic states (without considering the phonons) in the single excitation subspace are the photon-dressed ground state $|G,1\rangle$ and the single-molecule excited state $|E_n,0\rangle$. $|G,1\rangle$ is defined as the state where all the molecules are in the ground state and one photon is in the cavity

$$|G,1\rangle = |g_0\rangle \otimes ...|g_n\rangle ... \otimes |g_{N-1}\rangle \otimes |1\rangle, \tag{11}$$

and $|E_n,0\rangle$ is defined as the states where all the molecules are in the ground state except for the n_{th} molecule

$$|E_n,0\rangle = |g_0\rangle \otimes ...|e_n\rangle ... \otimes |g_{N-1}\rangle \otimes |0\rangle \tag{12}$$

In the single excitation manifold, we also have a collective "bright" excitonic state

$$|\mathrm{B},0\rangle = \frac{1}{\sqrt{N_a}} \sum_{n=0}^{N_a-1} |E_n,0\rangle \tag{13}$$

that couples to the $|G,1\rangle$ state through $\hat{H}_{\mathrm{LM}}$. This coupling leads to the polariton states $|\pm\rangle$, which are eigenstates of $\hat{H}_{\mathrm{S}}$, expressed as follows[87]

$$|+\rangle = \cos\theta |\mathrm{B},0\rangle + \sin\theta \, |G,1\rangle \tag{14a}$$
$$|-\rangle = -\sin\theta |\mathrm{B},0\rangle + \cos\theta \, |G,1\rangle, \tag{14b}$$

where the mixing angle is

$$\theta = \frac{1}{2} \tan^{-1} \left[\frac{2\sqrt{N_a} g_{\mathrm{c}}}{\omega_{\mathrm{c}} - \omega_a - \lambda} \right], \tag{15}$$

and the corresponding energies $\omega_\pm$ of the $|\pm\rangle$ states are

$$\omega_\pm = \frac{\omega_a + \lambda + \omega_c}{2} \pm \sqrt{N_a g_c^2 + \frac{(\omega_a + \lambda - \omega_c)^2}{4}}. \quad (16)$$

Furthermore, there exists $N_a - 1$ dark states $|\mathrm{D}_i\rangle$ that are given by[1]

$$|\mathcal{D}_\alpha\rangle = \sum_{n=1}^{N-1} C_{n,\alpha} |E_n, 0\rangle, \quad (17)$$

where the coefficients $C_{n,i}$ satisfy

$$\frac{1}{\sqrt{N}} \sum_{n=1}^{N-1} C_{n,\alpha} = \langle \mathrm{B}, 0 | \mathrm{D}_\alpha, 0\rangle = 0. \quad (18)$$

We note from Eq. 18 that since the dark states have no overlap with the collective "bright" states, they do not participate in the interaction with the cavity mode that is mediated by $\hat{H}_{\mathrm{LM}}$. Further, there is no optical transition from $|G, 0\rangle$ to $|\mathcal{D}_\alpha\rangle$, hence it is optically dark. The choice of dark state is not unique. For example, one can express them as follows[87,91]

$$|\mathrm{D}_\alpha\rangle = \frac{1}{\sqrt{N}} \sum_{n=1}^{N} \exp(-2\pi i \frac{n\alpha}{N}) |\mathrm{E}_n, 0\rangle, \quad (19)$$

where $\alpha \in \{1, \cdots, N-1\}$, which is fully delocalized among all N exciton states. Other choices are possible (see Eq. 8 in Ref. 92 for the Schur–Weyl basis).

The polariton states for the HTC model are outlined in Fig. 1. In the absence of exciton-phonon couplings, the $N-1$ dark states are energetically degenerate and have the same energies as the excitation energy of the bare molecule plus the reorganization energy, as shown in Fig. 1a. The upper and lower polaritons in resonance are also energetically separated from the dark states by an amount $\sqrt{N} g_{\mathrm{c}}$ when the system is in resonance ($\omega_{\mathrm{c}} = \omega_a + \lambda$). However, when there is light-matter detuning (*i.e.*, $\omega_{\mathrm{c}} \neq \omega_{\mathrm{a}} + \lambda$), the dark states are no longer separated in energy from the upper and lower polaritons by the same amount. In particular, with negative light-matter detuning ($\omega_{\mathrm{c}} < \omega_a + \lambda$), the dark states are closer in energy to the upper polariton state as illustrated in Fig. 1b. On the other hand, with positive detuning ($\omega_{\mathrm{c}} > \omega_a + \lambda$), the dark states are closer in energy to the lower polariton state as depicted in Fig. 1c. Thus, the polariton relaxation dynamics, mediated by exciton-phonon coupling in $\hat{H}_{\mathrm{SB}}$, will be affected by the energetics of the polariton and dark states due to different energy alignments caused by the light-matter detuning.

Note that the polariton state defined in Eq. 14 and the dark states in Eq. 17 are diabatic in nature, because there is no nuclear configuration dependence. In this case, the exciton-phonon couplings $\hat{H}_{\mathrm{SB}}$ will couple these polariton states and make transitions among them.[25,31] On the other hand, one can also choose to define $\hat{H}_{\mathrm{S}} + \hat{H}_{\mathrm{SB}}$ as the polariton Hamiltonian, whose eigenvector will be adiabatic polariton and dark states, and both of their characters will parametrically depend on the nuclear configuration.[26] In this case, the phonon fluctuation caused by $\hat{H}_{\mathrm{SB}}$ on polariton and dark states will be counted as the adiabatic polariton energy fluctuations, and the transitions among these adiabatic polariton and dark states are caused by the nuclear kinetic energy operators (as the derivative couplings). This is the picture used in the theoretical simulations in Ref. 26 (see Fig. 4 in that reference). Nevertheless, rigorous quantum mechanical descriptions of the dynamics (for all DOFs) will generate identical results in both pictures. Ehrenfest dynamics, as well as the mean-field-like approach (such as the mapping-based methods used in this work), are representation-independent, and thus generate identical results for both representations. The trajectory surface hopping approach, on the other hand, is not representation independent, and often performs the best in the adiabatic representation, so the adiabatic polariton Hamiltonian $\hat{H}_{\mathrm{pl}} = \hat{H}_{\mathrm{S}} + \hat{H}_{\mathrm{SB}}$ should be used in these surface hopping simulations.

Below, we briefly introduce the trajectory-based quantum dynamics approaches used in this work. Which we treat

$$\hat{R}_{k,n} = \sqrt{\frac{\hbar}{2\omega_k}} (\hat{\nu}_{k,n}^\dagger + \hat{\nu}_{k,n})$$
$$\hat{P}_{k,n} = i\sqrt{\frac{\hbar\omega_k}{2}} (\hat{\nu}_{k,n}^\dagger - \hat{\nu}_{k,n})$$

inside the $\hat{h}_{\mathrm{B}} + \hat{H}_{\mathrm{SB}}$ as the classical DOF, and we describe the polariton quantum subsystem in the diabatic basis of $\{|G, 1\rangle, |E_n, 0\rangle\}$ for Ehrenfes dynamics, γ-SQC, spin-LSC, and spin-PLDM approaches. For the surface hopping method, the adiabatic polariton states and dark states (see Ref. 26) are required, which are defined as the eigenstates of $\hat{H}_{\mathrm{pl}} = \hat{H}_{\mathrm{S}} + \hat{H}_{\mathrm{SB}}$ as follows

$$\hat{H}_{\mathrm{pl}}(\mathbf{R}) |\Psi(\mathbf{R})\rangle = \mathcal{E}(\mathbf{R}) |\Psi(\mathbf{R})\rangle.$$

A schematic illustration of the adiabatic polariton energy (and dark energy) can be found in Fig. 4 in Ref. 26. Note that for a large N in the single excitation subspace, diagonalizing the above equation is the computational bottleneck.

C. Non-adiabatic Mapping Dynamics Methods

In this section, we briefly discuss the mapping-based quantum dynamics approaches used in this work. Details of the standard Ehrenfest dynamics and surface hopping approaches are provided in the Supplemental Information. The common starting point of these mapping dynamics is the Meyer-Miller-Stock-Thoss (MMST) formalism,[56,64,65] which maps the discrete quantum DOF (described as discrete states) onto continuous phase space variables. A Hamiltonian in the diabatic representation

$\{|a\rangle\}$ is expressed as

$$\hat{H} = \frac{1}{2\mathbf{M}}\mathbf{P}^2 + U_0(\hat{\mathbf{R}}) \tag{20}$$

$$+ \sum_a V_{aa}(\hat{\mathbf{R}})|a\rangle\langle a| + \frac{1}{2}\sum_{b\neq a} V_{ab}(\hat{R})|a\rangle\langle b| \tag{21}$$

where $\hat{\mathbf{R}}$ and $\hat{\mathbf{P}}$ are the position and momenta for the nuclear DOFs respectively, $U_0(\hat{R})$ is the state-independent part of the Hamiltonian, and $V_{ab}(\hat{\mathbf{R}}) = \langle a|\hat{V}|b\rangle$. For the HTC model, we have

$$\hat{h}_{\rm B} = \frac{1}{2\mathbf{M}}\mathbf{P}^2 + U_0(\hat{\mathbf{R}}) \tag{22a}$$

$$\hat{H}_{\rm S} + \hat{H}_{\rm SB} = \hat{V} \tag{22b}$$

The MMST formalism maps the quantum Hamiltonian in Eq. 20 on to the following classical MMST Hamiltonian

$$\mathcal{H}_{\rm m} = \frac{1}{2\mathbf{M}}\mathbf{P}^2 + \frac{1}{2}\sum_{ab} V_{ab}(\mathbf{R})\left(p_a p_b + q_a q_b - 2\gamma_b\delta_{ab}\right) + U_0(\mathbf{R}) \tag{23}$$

where $2\gamma_b$ is viewed as a parameter[57] which specifies the zero-point energy (ZPE) of the mapping oscillators.[57,66,67,93] In principle, $2\gamma_b$ is state-specific and trajectory-specific.[80] The MMST mapping Hamiltonian has been historically justified by Stock and Thoss using the raising and lowering operators of a harmonic oscillator as the mapping operator.[64,65] Recently, a more natural mapping has been derived using the $SU(N)$ Lie group theory or so-called generalized spin mapping approach,[81] which is connected to the MMST mapping approach.[67,81]

Classical trajectories are generated based on Hamilton's equations of motion (EOM) for $\mathcal{H}_{\rm m}$

$$\dot{q}_b = \partial\mathcal{H}_{\rm m}/\partial p_b; \quad \dot{p}_a = -\partial\mathcal{H}_{\rm m}/\partial q_a \tag{24a}$$

$$\dot{\mathbf{R}} = \partial\mathcal{H}_{\rm m}/\partial\mathbf{P}; \quad \dot{\mathbf{P}} = -\partial\mathcal{H}_{\rm m}/\partial\mathbf{R} = \mathbf{F}, \tag{24b}$$

with the nuclear force expressed as

$$\mathbf{F} = -\frac{1}{2}\sum_{ab}\nabla U_{ab}(\mathbf{R})\left(p_a p_b + q_a q_b - 2\gamma_b\delta_{ab}\right) - \nabla U_0(\mathbf{R}). \tag{25}$$

The above classical EOM for both mapping variables (for the quantum subsystem) and the classical DOFs are propagated using the velocity Verlet algorithm.

The γ-SQC approach. The γ-SQC approach samples the initial electronic condition and estimates the population based on the action-angle variables, $\{\varepsilon_b, \theta_b\}$, expressed as follows

$$\varepsilon_b = \frac{1}{2}\left(p_b^2 + q_b^2\right); \quad \theta_b = -\tan^{-1}\left(\frac{p_b}{q_b}\right). \tag{26}$$

They are inversely related to the mapping variables as follows

$$q_b = \sqrt{2\varepsilon_b}\cos(\theta_b); \quad p_b = -\sqrt{2\varepsilon_b}\sin(\theta_b), \tag{27}$$

where ε_b is a positive-definite action variable that is directly proportional to the mapping variables' radius in action space.[80]

The SQC approach calculates the population of electronic state $|b\rangle$, which will be evaluated as[57]

$$\rho_{bb}(t) = {\rm Tr}_{\mathbf{R}}\left[\hat{\rho}(0)e^{i\hat{H}t/\hbar}|b\rangle\langle b|e^{-i\hat{H}t/\hbar}\right] \tag{28}$$

$$\approx \int d\boldsymbol{\tau}\rho_{\rm W}(\mathbf{P},\mathbf{R})W_a(\boldsymbol{\varepsilon}(0))W_b(\boldsymbol{\varepsilon}(t)),$$

where $\hat{\rho}(0) = \hat{\rho}_{\mathbf{R}} \otimes |a\rangle\langle a|$ is the initial density operator, $\rho_{\rm W}(\mathbf{P},\mathbf{R})$ is the Wigner transform of $\hat{\rho}_{\mathbf{R}}$ operator for the nuclear DOFs, $\boldsymbol{\varepsilon} = \{\varepsilon_1, \varepsilon_2, ..., \varepsilon_{\mathcal{N}}\}$ is the positive-definite action variable vector for $\mathcal{N}$ electronic states,[80] $W_a(\boldsymbol{\varepsilon}) = \delta(\varepsilon_a - (1+\gamma_a))\prod_{a\neq b}\delta(\varepsilon_b - \gamma_b)$ is the Wigner transformed action variables,[94] and $d\boldsymbol{\tau} \equiv d\mathbf{P}\cdot d\mathbf{R}\cdot d\boldsymbol{\varepsilon}\cdot d\boldsymbol{\theta}$. For practical reasons, the delta functions above in $W_a(\boldsymbol{\varepsilon})$ are broadened using a distribution function (so-called window function) that is used to bin the resulting electronic action variables in action-space.[57] Here, we used the triangle window[80,94] which is expressed as

$$W_b(\boldsymbol{\varepsilon}) = w_1(\varepsilon_b)\prod_{b'\neq b}^{\mathcal{N}} w_0(\varepsilon_b, \varepsilon_{b'}), \tag{29}$$

where the window functions are defined as

$$w_1(\varepsilon) = \begin{cases} (2-\varepsilon)^{2-\mathcal{N}}, & 1 < \varepsilon < 2 \\ 0, & \text{else} \end{cases} \tag{30}$$

and

$$w_0(\varepsilon, \varepsilon') = \begin{cases} 1, & \varepsilon' < 2-\varepsilon \\ 0, & \text{else}, \end{cases} \tag{31}$$

and trajectories are assigned to state b at time t if $\varepsilon_b \geq 1$ and $\varepsilon_{b'} < 1$ for all $b' \neq b$.

The time-dependent population of the state $|b\rangle$ is computed with Eq. 28. Using the window function estimator, the total population is no longer properly normalized due to the fraction of trajectories that are outside of any window region at any given time.[60] Thus, the total population must be normalized[60] with the following procedure

$$\rho_{bb}(t)/\sum_{a=1}^{N}\rho_{aa}(t) \to \rho_{bb}(t). \tag{32}$$

In the γ-SQC approach,[80] it was proposed that the mapping ZPE should be chosen in such a way as to constrain the initial force to be composed purely of the initially occupied state.[80] The basic logic of γ-SQC is to choose a γ_b for each state $|b\rangle$ in every given individual trajectory, such that the initial population is forced to respect the initial electronic excitation focused onto a single excited state. If the initial electronic state is $|a\rangle$, then

$$\gamma_b = \varepsilon_b - \delta_{ba}, \tag{33}$$

or equivalently,

$$\delta_{ba} = \varepsilon_b - \gamma_b, \tag{34}$$

where the $\{\varepsilon_b\}$ are uniformly sampled inside the window function (Eq. 29), and following that the γ_b are chosen to satisfy Eq. 34.

These γ_b will be explicitly used in the EOMs in Eqs. 24-25, and in particular, the nuclear forces become

$$\mathbf{F} = -\frac{1}{2}\sum_{ab} \nabla V_{ab}(\mathbf{R})\big(p_a p_b + q_a q_b - 2\gamma_b \delta_{ba}\big), \tag{35}$$

ensuring the initial forces (at $t = 0$) are simply $\mathbf{F} = -\nabla V_{aa}(\mathbf{R})$. Previously, without any adjustments to γ_b, the chosen values for γ_b were only dependent on the windowing function itself, *i.e.*, $\gamma_b = 0.366$ for the square windows and $\gamma_b = 1/3$ for the triangle windows. With the above γ-correction method,[80] each individual trajectory will have its own state-specific γ_b for state $|b\rangle$ that is completely independent of the choice of window function. This method has been proven to provide very accurate non-adiabatic dynamics in model photo-dissociation problems (coupled Morse potential), and has outperformed fewest-switches surface hopping (FSSH) with decoherence correction in *ab initio* on-the-fly simulations.[74,75]

The Spin-LSC method. For the spin-LSC approach,[66,67] one chooses a universal ZPE parameter $2\gamma_b = \Gamma$ for all states and trajectories. The spin-LSC population dynamics is calculated as

$$\begin{aligned}\rho_{bb}(t) &= \mathrm{Tr}_{\mathbf{R}}\left[\hat{\rho}_R \otimes |a\rangle\langle a| e^{i\hat{H}t/\hbar}|b\rangle\langle b| e^{-i\hat{H}t/\hbar}\right] \\ &\approx \int d\boldsymbol{\tau}\, \rho_{\mathrm{W}}(\mathbf{P},\mathbf{R}) \big[|a\rangle\langle a|\big]_{\mathrm{s}}(0) \cdot \big[|b\rangle\langle b|\big]_{\bar{\mathrm{s}}}(t),\end{aligned} \tag{36}$$

where the population estimators are obtained from the Stratonovich-Weyl transformed electronic projection operators, with the expressions as follows[67]

$$\big[|a\rangle\langle a|\big]_{\mathrm{s}} = \frac{1}{2}(q_a^2 + p_a^2 - \Gamma) \tag{37a}$$

$$\big[|b\rangle\langle b|\big]_{\bar{\mathrm{s}}} = \frac{\mathcal{N}+1}{2(1+\frac{\mathcal{N}\Gamma}{2})^2}\cdot(q_b^2+p_b^2) - \frac{1-\frac{\Gamma}{2}}{1+\frac{\mathcal{N}\Gamma}{2}}. \tag{37b}$$

The parameter Γ is related to the radius of the generalized Bloch sphere r_{s} through $\Gamma = \frac{2}{\mathcal{N}}(r_{\mathrm{s}} - 1)$, where s and $\bar{\mathrm{s}}$ are complementary indices in the Stratonovich-Weyl transform. Among the vast parameter space, one of the best-performing choices[66,67] is when $r_{\mathrm{s}} = r_{\bar{\mathrm{s}}} = \sqrt{\mathcal{N}+1}$, which is referred to as $\mathrm{s} = \mathrm{W}$, leading to a ZPE parameter

$$\Gamma = \frac{2}{\mathcal{N}}(\sqrt{\mathcal{N}+1} - 1), \tag{38}$$

as well as the identical expression of $[|a\rangle\langle a|]_{\mathrm{s}}$ and $[|b\rangle\langle b|]_{\bar{\mathrm{s}}}$ in Eq. 37. We further use the focused initial condition[66,67] that replaces the sampling of the mapping variables in the $d\boldsymbol{\tau}$ integral of Eq. 36 with specific values of the mapping variables, such that $\frac{1}{2}(q_a^2+p_a^2-\Gamma) = 1$ for initially occupied state $|a\rangle$ and $\frac{1}{2}(q_b^2+p_b^2-\Gamma) = 0$ for the initially unoccupied states $|b\rangle$. The angle variables $\{\theta_b\}$ (Eq. 26) are randomly sampled[67] in the range of $[0, 2\pi)$. More computational details for the γ-SQC and spin-LSC are provided in section III B.

III. COMPUTATIONAL DETAILS

Initial Conditions. We describe the details of the HTC models used in our benchmark and the corresponding initial condition for the dynamics. The initial condition for all our simulations is assumed to be separable, and hence, the density matrix $\hat{\rho}$ is given by

$$\hat{\rho} = \hat{\rho}_{\mathrm{S}} \otimes \frac{e^{-\beta\hat{h}_{\mathrm{B}}}}{\mathcal{Z}_{\mathrm{B}}}, \tag{39}$$

where $\hat{\rho}_{\mathrm{S}}$ is the system reduced density operator, $\beta = 1/k_{\mathrm{B}}T$ is the inverse temperature, and $\mathcal{Z}_{\mathrm{B}} = \mathrm{Tr}[e^{-\beta\hat{h}_{\mathrm{B}}}]$ is the bare-bath partition function. In Eq. 39, we assume that the bath is in thermal equilibrium so that the bath reduced density matrix operator takes the form of a Boltzmann distribution. Also, the system is initially placed in the upper polariton state $|\Psi(0)\rangle = |+\rangle$ and the associated system reduced density operator is given by $\hat{\rho}_{\mathrm{S}} = |+\rangle\langle+|$. This initial state is chosen so that we can observe the relaxation from the upper polariton state to the dark states and lower polariton state because of exciton-phonon coupling.

Model Parameters. We construct six HTC benchmark models to investigate the performance of the trajectory-based non-adiabatic methods to simulate polariton relaxation dynamics. These models scan a range of the following physical parameters: (1) number of molecules (N_a), (2) light-matter detuning ($\omega_{\mathrm{c}} - \omega_a - \lambda$), (3) single-molecule coupling strength (g_{c}), (4) reorganization energy (λ), (5) bath cutoff frequency (ω_ν), and (6) temperature ($\beta = 1/k_{\mathrm{B}}T$).

In each model, we vary one parameter and fix the other five parameters. The values of these parameters for all six models are provided in Table 1. We note that by changing the parameters in models 1 to 3, the polariton relaxation dynamics are affected through the system contribution to the Hamiltonian, while in changing the parameters in models 4 to 6, the dynamics are affected through the system-bath interaction term. Furthermore, the results for models 1 to 4 are presented in the main text below, while models 5 and 6 are provided in Sec. III of the Supplementary Material.

A. Details of the HEOM Simulations

For the model we considered, the molecular phonon bath is described by the Drude-Lorentz spectral density,

Table 1. The parameters assigned in different models used in this work. The results from model 1 to model 4 are presented in the main text, while the results of model 5 and model 6 are presented in the supplementary information.

Model	N_a	$\omega_c - \omega_a - \lambda$ (meV)	g_c (meV)	λ (meV)	ω_ν (meV)	β (a.u)
1	5/10/15	0	68.1	30	24.8	1000
2	10	-200/0/200	68.1	30	24.8	1000
3	10	0	40.8/68.1/96.1	30	24.8	1000
4	10	0	68.1	10/30/50	24.8	1000
5	10	0	68.1	30	12.4/24.8/37.2	1000
6	10	0	68.1	30	24.8	250/1000/4000

so that its time-correlation function (TCF) decomposition is computed using the Padé spectral decomposition (PSD) scheme.[95–97] Here, we use the $[N-1/N]$ scheme[97] with 2 low-temperature correction terms. For HEOM propagation, we use the fourth order Runge-Kutta (RK-4) integrator with a time step of 0.005 fs, together with the on-the-fly filtering algorithm[98] with an error tolerance of 1×10^{-6}. The number of tiers is set as 20. The convergence of the calculation is carefully checked with the above parameters. Also, a factorizable initial full-density matrix is applied, which is the same as Eq. 39. Details about the HEOM method are provided in Sec. I of the Supplementary Material.

B. Details of the Trajectory-based Dynamics

To perform the γ-SQC dynamics, we need to sample the initial condition for the quantum subsystem. In this work, we sample the action-angle variables $\{\varepsilon_b, \theta_b\}$ and subsequently transform them to the mapping variables$\{p_b, q_b\}$ using Eq. 27. The action variables $\{\varepsilon_b\}$ are sampled according to the window function in Eq. 29, and the angle variables $\{\theta_b\}$ are randomly sampled from $[0, 2\pi)$. The triangle window is used in this work, although the square window generates similar results.

For the spin-LSC dynamics, we use the focused initial conditions[67] as described in section II C, where the action variable ε_a is set to be $1+\Gamma/2$ for the initially occupied state and $\Gamma/2$ for the initially unoccupied state, with Γ expressed in Eq. 38. The angle variables $\{\theta_b\}$ are randomly generated between $[0, 2\pi)$ as in the γ-SQC method. The canonical mapping variables are obtained from Eq. 27.

The initial nuclear distribution of all trajectory-based simulations (Ehrenfest, GFSH, γ-SQC, and spin-LSC) are generated by sampling the Wigner density

$$[\langle R|\chi\rangle]_w = \frac{1}{\hbar\pi} e^{-M(P^2+\omega_0^2(R-R_0)^2)/\omega_0\hbar}, \qquad (40)$$

which is the Wigner transformation of the nuclear wavefunction $\chi(R) = \langle R|\chi\rangle$ in the initial state. Here, R and P are the nuclear coordinate and momentum, respectively. The nuclear time step used in all the trajectory-based simulations is $dt = 3.0$ a.u., with 200 equally spaced time steps for the mapping variables' integration during each nuclear time step. The equation of motion in Eq. 24-Eq. 25 are integrated using a second-order symplectic integrator for the MMST variables[99,100]. The population dynamics using all trajectory-based methods were averaged over 10000 trajectories.

IV. RESULTS

In Fig. 2, we present the population dynamics of the polariton states and the dark states for model 1, which varies the number of molecules N_a from 5 molecules to 15 molecules while keeping the other parameters fixed. The trajectory-based methods are depicted using open circles and are compared to numerically exact results (HEOM) depicted using solid lines. We can see that in Figs. 2a-2l, all trajectory-based methods are able to semi-quantitatively account for the relaxation of the upper polariton (UP) state into the dark states (DS), and eventually to the lower polariton (LP) state. However, both mixed quantum-classical (MQC) methods, Ehrenfest, and global flux surface hopping (GFSH) predict a slower relaxation rate and a larger steady-state population (see Fig. 2a-Fig. 2f) for the upper polariton state compared to the HEOM results. Focusing on the transitions into and out of the dark states, we observe that both MQC methods are only able to qualitatively capture the increase in the total dark state populations. After the dark state populations have reached a maximum value, both MQC methods predict little changes in the dark state population, which is in contrast to numerically exact results from the HEOM simulation. As a result, the increase in lower polariton population calculated from both MQC methods, which comes through the transitions from the dark states, is smaller than that predicted by the HEOM method.

On the other hand, the mapping-based methods (γ-SQC and spin-LSC) show much more accurate relaxation dynamics from the upper polariton state, compared to the HEOM results, and the steady-state population for the upper polariton is also similar to the exact HEOM dynamics (Fis. 2g-2l). We also observe that the transitions into the dark states are better captured with these mapping-based methods, although the γ-SQC method (Fig. 2g-Fig. 2i) slightly outperforms the spin-LSC method (Fig. 2j-Fig. 2l) in predicting the longer time transitions from the dark states to the lower polari-

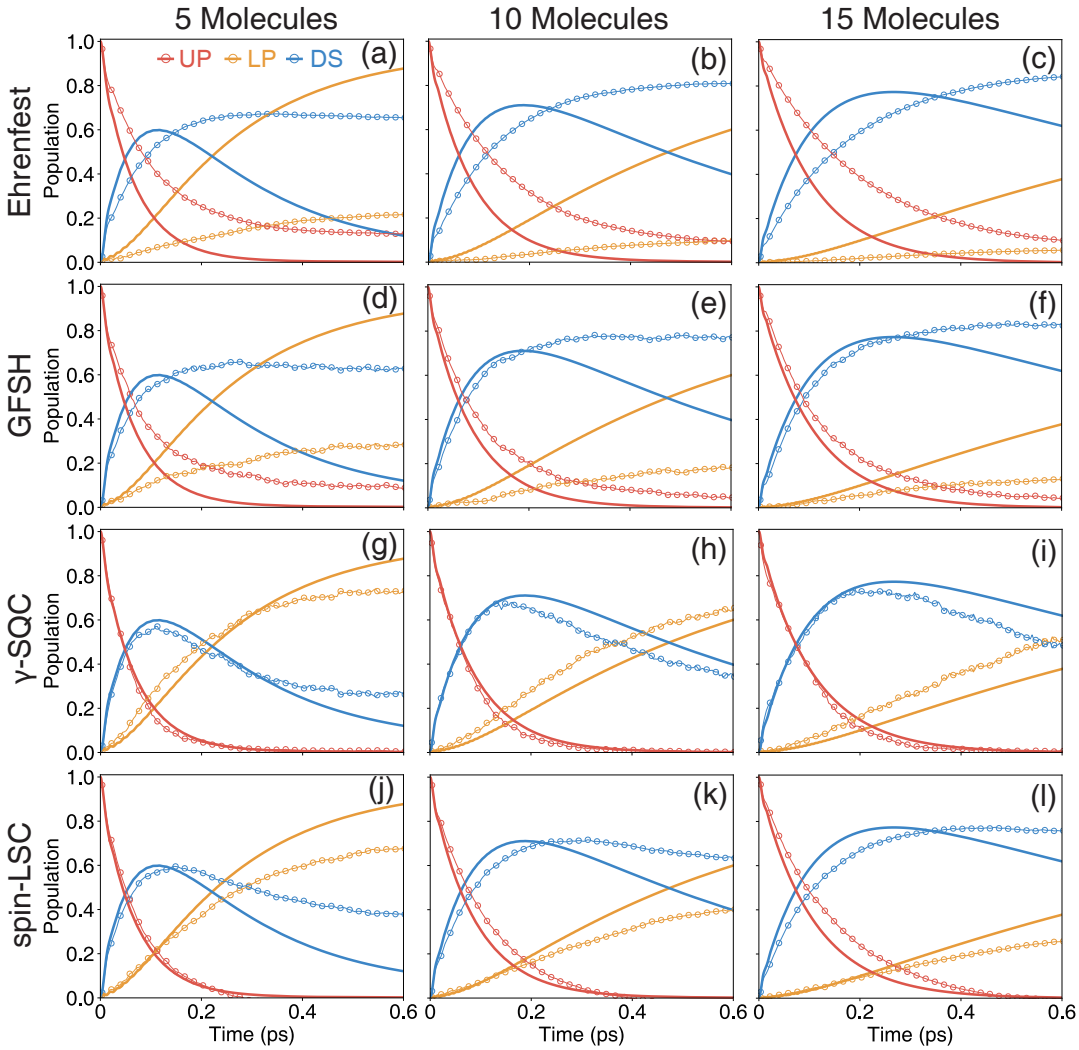

Figure 2. Population dynamics of the upper polaritonic state (UP), lower polaritonic state (LP), and sum over all dark states (DS) for the HTC model computed with different MQC dynamics methods, including Ehrenfest, GFSH, γ-SQC, and spin-LSC. Different numbers of molecules ($N_a = 5/10/15$) are used in the dynamics simulations. The cavity frequency is $\omega_c = 2.0$ eV, the light-matter coupling strength is $g_c = 68.1$ meV, the reorganization energy is $\lambda = 30$ meV, the temperature is $\beta = 1000$ a.u. and the cutoff frequency during the initial sampling process is ω_ν=24.8 meV. See Model 1 in Table 1.

ton states. Further, the population of the lower polariton state computed from the mapping-based method is also comparable to the populations predicted from the HEOM method.

Fig. 3 presents the population dynamics of the polariton states and the dark states for model 2, where the light-matter detuning $\omega_c - \omega_a - \lambda$ varies from negative to positive values, while keeping the other parameters fixed. In Fig. 3, all trajectory-based methods are able to qualitatively account for the relaxation of the upper polariton state into the other states. However, both MQC methods (Ehrenfest and GFSH) predict a slower relaxation rate and a larger steady-state population for the upper polariton state compared to the HEOM results. Looking at the transitions into and out of the dark states, we observe that both MQC methods are only able to qualitatively capture the increase in the total dark state populations due to relaxation from the upper polariton state in the short time regime (up to 0.1 ps). One exception to this observation about the dark states is given in Fig. 3d, where the GFSH method predicts comparable dark state populations compared to the HEOM method for negative detuning ($\omega_c - \omega_a - \lambda = -200$ meV). For the lower polariton populations, both MQC methods consistently underestimate the populations compared to the HEOM method.

The mapping-based methods (γ-SQC and spin-LSC), again, show more accurate results that are comparable to the HEOM method, and the steady-state population for the upper polariton is also similar to the HEOM method. We also observe that the transitions into the dark states are better captured with the mapping-based methods,

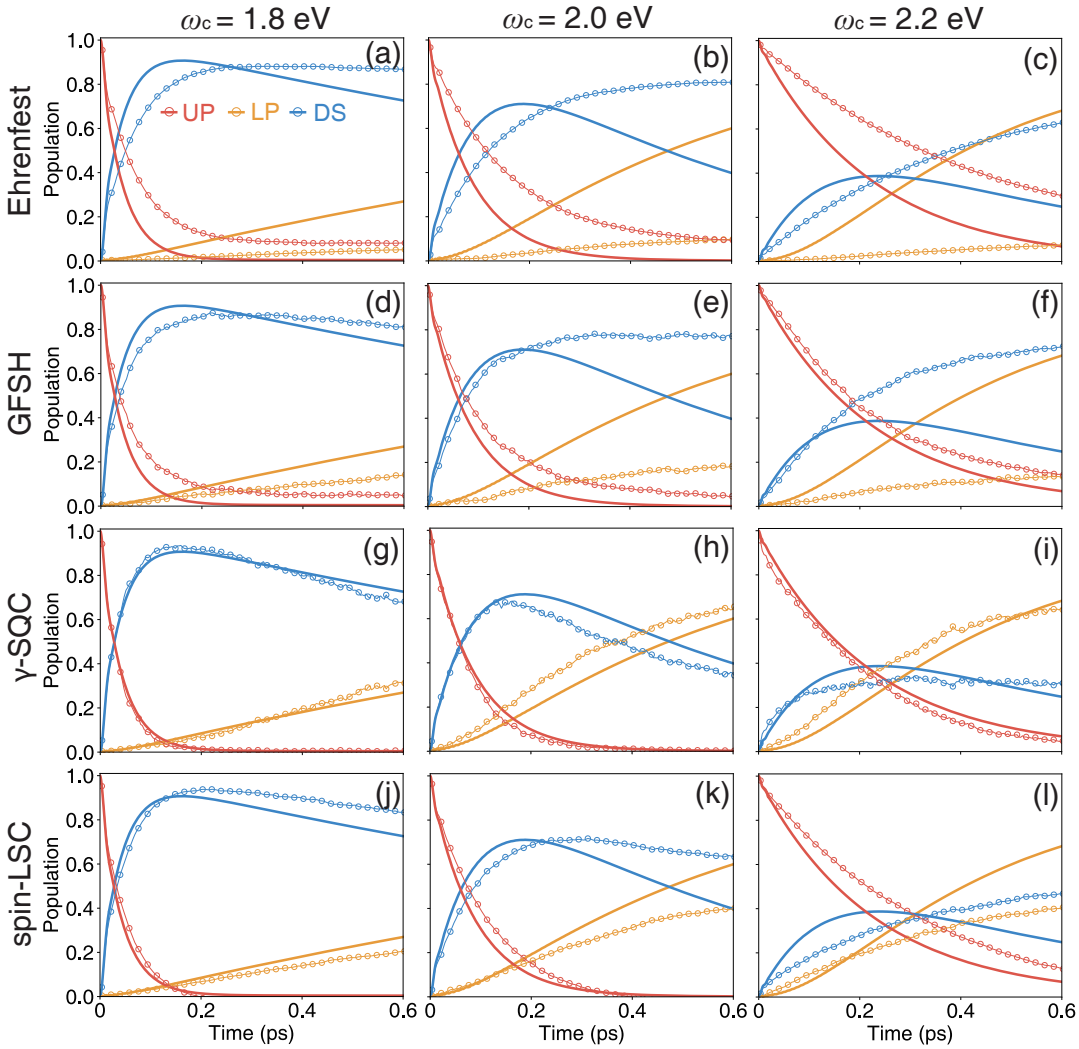

Figure 3. Population dynamics of the upper polaritonic state (UP), lower polaritonic state (LP), and sum over all dark states (DS) for the HTC model computed with different MQC dynamics methods, including Ehrenfest, GFSH, γ-SQC, and spin-LSC. Different cavity frequencies ($\omega_c = 1.8, 2.0, 2.2$ eV) are used in the dynamics simulations. The number of molecules is $N_a = 10$, the light-matter coupling strength is $g_c = 68.1$ meV, and the reorganization energy is $\lambda = 30$ meV. See Model 2 in Table 1 for details.

although the γ-SQC method outperforms the spin-LSC method again in predicting the longer time transitions from the dark states to the lower polariton states. Further, we note that the population of the lower polariton state computed via the γ-SQC method is comparable to the populations predicted from the HEOM method, while the population of the lower polariton state computed from the spin-LSC method is consistently lower than that from the HEOM method.

Fig. 4 presents the population dynamics of the polariton states and the dark states for model 3, which varies the single-molecule coupling strength g_c from 40.8 meV to 96.1 meV, while keeping the other parameters fixed. Again, all trajectory-based methods are able to qualitatively account for the relaxation of the upper polariton state into the other states. However, both MQC methods (MFE and GFSH) predict a slower relaxation rate and a larger steady-state population for the upper polariton state compared to the HEOM results. Looking at the transitions into and out of the dark states, we observe that both MQC methods are only able to qualitatively capture the increase in the total dark state populations. After the dark state populations have reached a maximum value, both MQC methods predict little changes in the dark state population, which is in contrast to numerically exact results from the HEOM method. Consequently, the lower polariton population calculated from both MQC methods is consistently underestimated compared to the HEOM method.

In contrast, the mapping-based methods (γ-SQC and spin-LSC) show more accurate relaxation rates for the upper polariton state compared to the HEOM method,

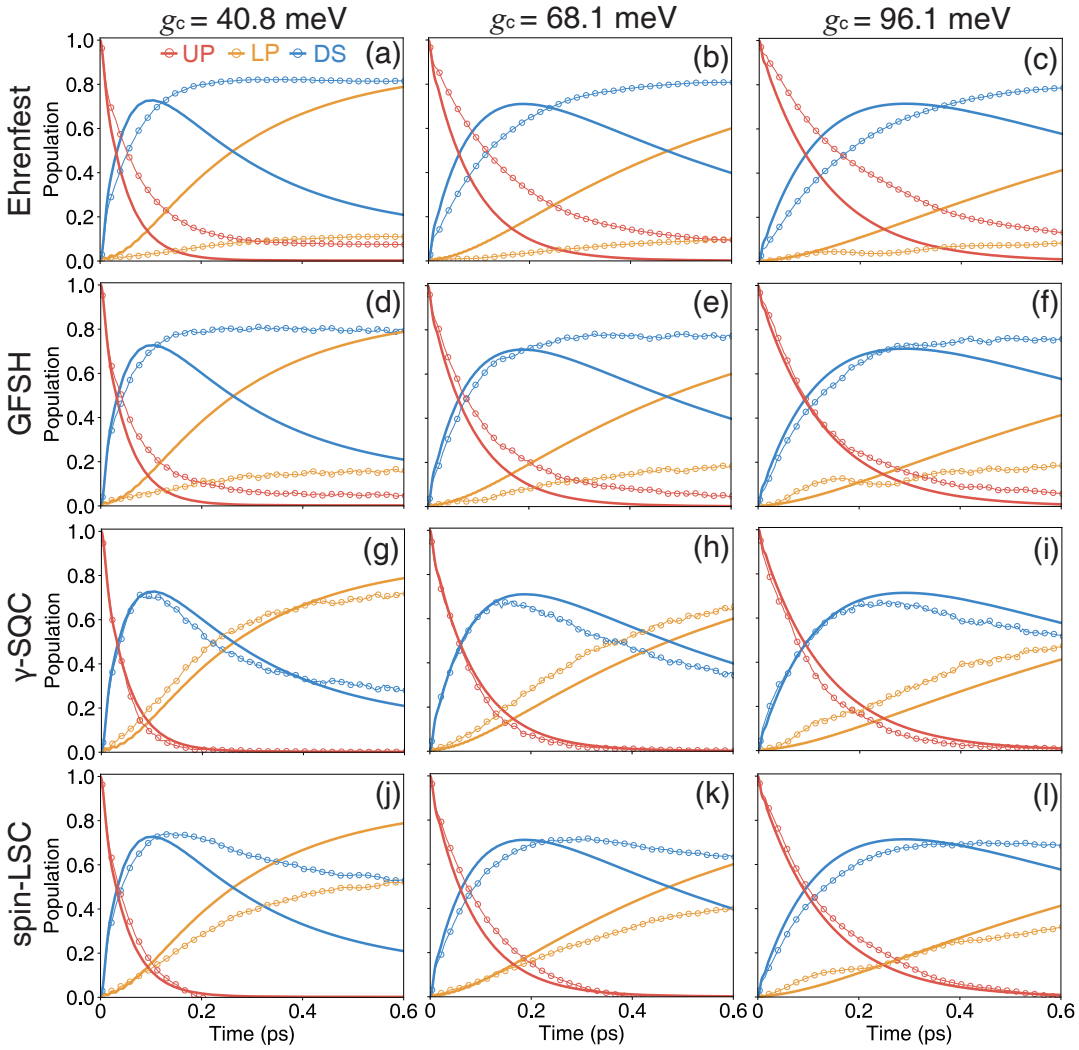

Figure 4. Population dynamics of the upper polaritonic state (UP), lower polaritonic state (LP), and sum over all dark states (DS) for the HTC model computed with different MQC dynamics methods, including Ehrenfest, GFSH, γ-SQC, and spin-LSC. Different light-matter coupling strengths (g_c = 40.8/68.1/96.1 meV) are used in the dynamics simulations. The number of molecules is $N_a = 10$, the cavity frequency is $\omega_c = 2.0$ eV, and the reorganization energy is $\lambda = 30$ meV. See Model 3 in Table 1 for details.

and the steady-state population for the upper polariton is also similar to the HEOM method. We also observe that the transitions into the dark states are better captured with the mapping-based methods, and the γ-SQC method again outperforms the spin-LSC method in predicting the longer time transitions from the dark states to the lower polariton states. For the population of the lower polariton state, we note that the γ-SQC method tends to overestimate the population compared to the HEOM method, while the spin-LSC method tends to underestimate the population compared to the HEOM method.

In Figure 5, we present the population dynamics of the polariton states and the dark states for model 4, which varies the reorganization energy λ from 10 meV to 50 meV while keeping the other parameters fixed. All trajectory-based methods are able to qualitatively account for the relaxation of the upper polariton state into the other states. However, both MQC methods (Ehrenfest and GFSH) predict a slower relaxation rate and a larger steady-state population for the upper polariton state compared to the HEOM results. For $\lambda = 10$ meV and $\lambda = 30$ meV (Fig. 5a, Fig. 5b, Fig. 5d and Fig. 5e), both MQC methods predict little changes in the dark state population after the dark state populations have reached a maximum value, which is in contrast to numerically exact results from the HEOM method. On the other hand, for $\lambda = 50$ meV (Fig. 5c and Fig. 5f), the MQC methods underestimate the populations of the dark states as compared to the HEOM method. As a result, the increase in lower polariton population calculated from both MQC methods, which comes through the

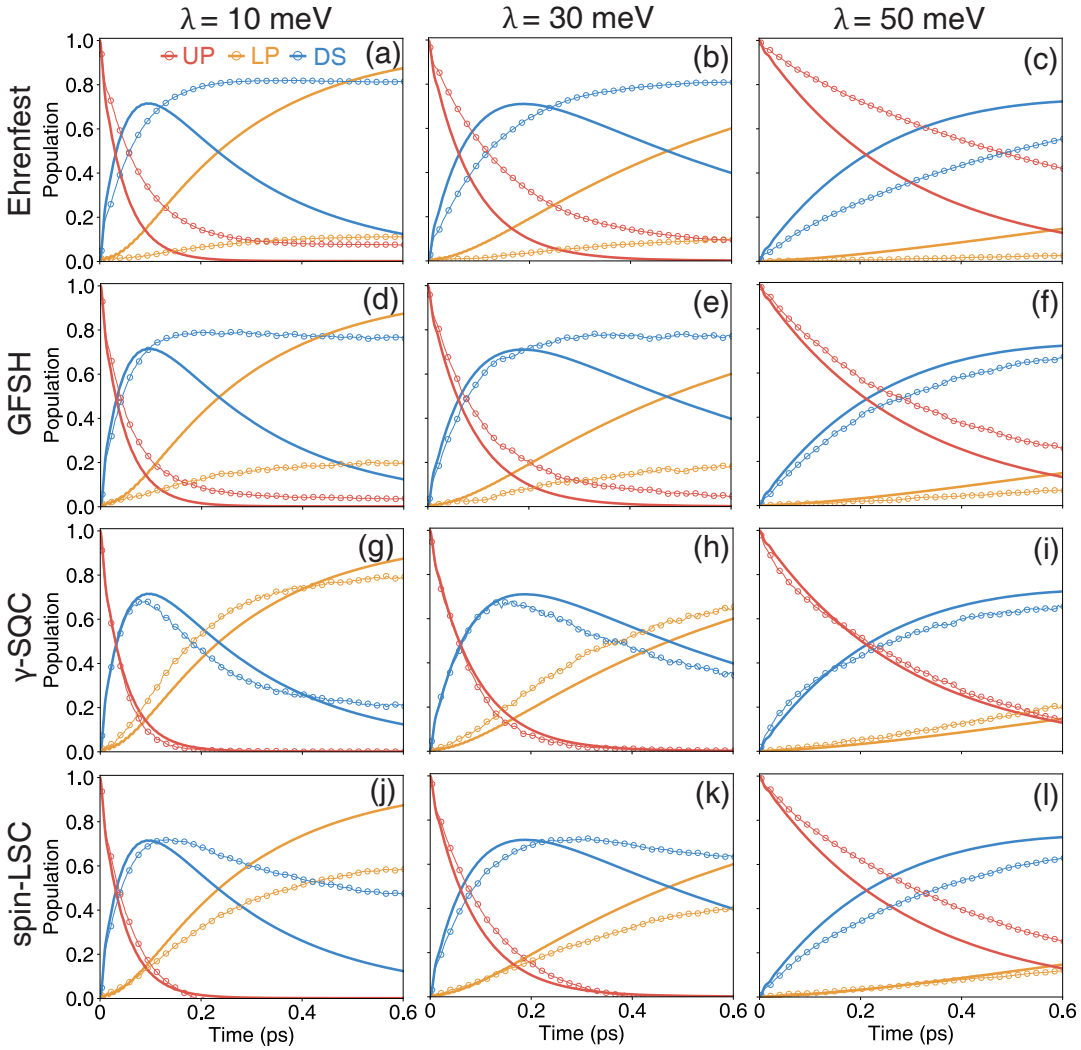

Figure 5. Population dynamics of the upper polaritonic state (UP), lower polaritonic state (LP), and sum over all dark states (DS) for the HTC model computed with different MQC dynamics methods, including Ehrenfest, GFSH, γ-SQC, and spin-LSC. Different reorganization energy ($\lambda = 10/30/50$ meV) are used in the dynamics simulations. The number of molecules is $N_a = 10$, and the cavity frequency is $\omega_c = 2.0$ eV. See Model 4 in Table 1 for details.

transitions from the dark states, is always smaller than that predicted by the HEOM method.

The mapping-based methods (γ-SQC and spin-LSC) show more reliable relaxation rates for the upper polariton state compared to the HEOM method and the steady-state population for the upper polariton is also similar to the HEOM method for $\lambda = 10$ meV and $\lambda = 30$ meV (Fig. 5g, Fig. 5h, Fig. 5j, and Fig. 5k). We also observe that the transitions into the dark states are better captured with the mapping-based methods, and the γ-SQC method outperforms the spin-LSC method in predicting the longer time transitions from the dark states to the lower polariton states. Consequently, the population of the lower polariton state computed from the mapping-based method is also comparable to the populations predicted from the HEOM method.

Further benchmark results for model 5 and model 6 are provided in the Supplemental Materials, with changing bath characteristic frequency ω_ν (Fig. S1 for model 5) and temperature T (Fig. S2 for model 6). All methods show qualitatively correct dynamics, and the mapping methods are more accurate than the MQC approaches, and γ-SQC slightly outperforms spin-LSC.

Finally, in Fig. 6, we present a further comparison of the polariton relaxation dynamics computed using the spin-PLDM approach[69,70] for model 1. The theoretical details of this approach can be found in Ref. 69. Similar to the original PLDM approach,[58,59] spin-PLDM explicitly accounts for the forward and backward propagators of the quantum subsystem, using the forward and backward mapping variables. One can see in Fig. 6 that spin-PLDM provides more accurate results compared to spin-LSC and achieves an accuracy at a similar level of γ-SQC (see Fig. 2g-h). However, being a partially forward

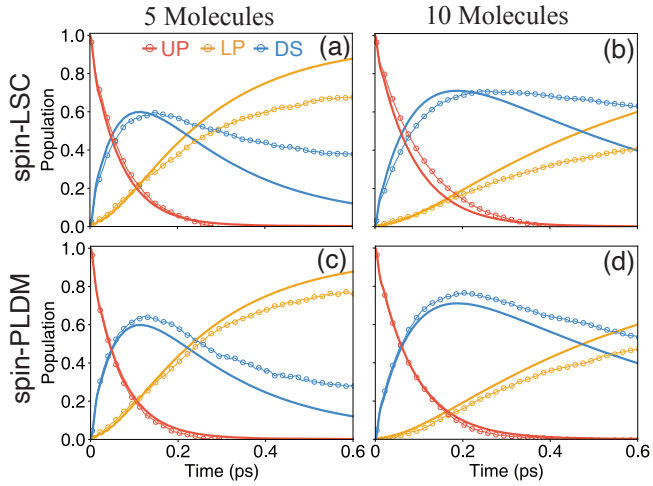

Figure 6. Same as Fig. 1, by comparing results obtained from spin-LSC and spin-PLDM.

and backward method, the computational cost of spin-PLDM is significantly increased compared to the Ehrenfest method and all linearized mapping approaches (γ-SQC and spin-LSC).

V. CONCLUSIONS

In this paper, we provide several benchmark results for various trajectory-based non-adiabatic simulations on polariton relaxation dynamics. The non-adiabatic methods we use in our benchmark are well-known in the literature, such as MQC-based methods and the recently developed mapping-based methods (both γ-SQC and spin-mapping representation). In particular, we showed that the MQC-based methods (MFE and GFSH) are able to qualitatively capture the initial relaxation dynamics of the polaritonic system but are unable to accurately describe subsequent relaxation to the dark states and the lower polariton states. The spin-mapping method that we chose (spin-LSC) markedly improves on the MQC-based methods in terms of simulating the relaxation dynamics of polaritons, although it is unable to capture the correct rates of relaxation from the dark states to the lower polariton state. In comparison with the other three methods, we find that the γ-SQC method is able to accurately capture all relevant relaxation dynamics of the polariton system, including the transition from dark state to lower polariton states at long time scales. Thus, for the models investigated in this work, we see that the γ-SQC method outperforms the other three methods to describe the relevant polariton physics in the HTC model. Despite this observation, more work remains to be done to theoretically investigate the limitations of the other trajectory-based methods and address their shortcomings in terms of simulating the relevant dynamics for polariton chemistry and physics. We further envision that our benchmark results will provide useful information to the emergent polariton chemistry and physics community by showcasing the applicability of various trajectory-based methods to analyze problems of interest, such as polariton photochemical processes and polariton transport dynamics.

As we approach the large N_a limit with $N_a \sim 10^6$, which is considered the experimentally relevant regime,[1] we note that one should take advantage of the well-known mean-field solution[101,102] or the recently proposed CUT-E approach[103,104] (for the zero-temperature case and with a single high-frequency vibration mode per molecule) that effectively only treats one or a few molecules. We can also exploit the sparsity of the HTC Hamiltonian[24] to enable direct simulations of $N_a \sim 10^6$ molecules coupled to a single cavity mode in the single excitation subspace with trajectory-based methods. One could also explore using the relatively short memory kernel time compared to the density matrix dynamics time to facilitate the simulations.[105,106] These directions remain to be explored in the future.

AUTHOR CONTRIBUTIONS

† D.H. and B. X. K. C contributed equally to this work.

ACKNOWLEDGMENTS

This work was supported by the National Science Foundation Award under Grant No. CHE-2244683 and OAC-2311442. D.H. is supported by the National Science Fund of China (No. 22403008), the Beijing Natural Science Foundation (No. 2244074) and the start-up funding (No. 312200502511) from the Beijing Normal University at Zhuhai. W.Y. appreciates the support of his Esther M. Conwell Graduate Fellowship at the University of Rochester. P.H. appreciates the support of the Cottrell Scholar Award (a program by the Research Corporation for Science Advancement). Computing resources were provided by the Center for Integrated Research Computing (CIRC) at the University of Rochester, and by the Interdisciplinary Intelligence SuperComputer Center of Beijing Normal University at Zhuhai. We appreciate valuable comments on the manuscript from Eric Koessler.

CONFLICT OF INTEREST

The authors have no conflicts to disclose.

SUPPLEMENTARY MATERIAL

See Supplementary Material for details about the HEOM method, the Ehrenfest dynamics, the Global Flux Surface Hopping non-adiabatic methods used to perform

the benchmark simulations, and polariton relaxation dynamics for models 5 and 6.

AVAILABILITY OF DATA

The data that support the findings of this study are available from the corresponding authors upon a reasonable request.

REFERENCES

[1]A. Mandal, M. A. Taylor, B. M. Weight, E. R. Koessler, X. Li, and P. Huo, Chemical Reviews **123**, 9786 (2023).
[2]J. Feist, J. Galego, and F. J. Garcia-Vidal, ACS Photonics **5**, 205 (2018).
[3]A. Mandal and P. Huo, J. Phys. Chem. Lett. **10**, 5519 (2019).
[4]H. L. Luk, J. Feist, J. J. Toppari, and G. Groenhof, J. Chem. Theory Comput. **13**, 4324 (2017).
[5]G. Groenhof and J. J. Toppari, J. Phys. Chem. Lett. **9**, 4848 (2018).
[6]G. Groenhof, C. Climent, J. Feist, D. Morozov, and J. J. Toppari, J. Phys. Chem. Lett. **10**, 5476 (2019).
[7]R. H. Tichauer, J. Feist, and G. Groenhof, J. Chem. Phys. **154**, 104112 (2021).
[8]T. W. Ebbesen, Acc. Chem. Res. **49**, 2403 (2016).
[9]M. Kowalewski and S. Mukamel, Proc. Natl. Acad. Sci. U.S.A. **114**, 3278 (2017).
[10]J. Flick, M. Ruggenthaler, H. Appel, and A. Rubio, Proc. Natl Acad. Sci. USA **114**, 3026 (2017).
[11]R. F. Ribeiro, L. A. Martínez-Martínez, M. Du, J. Campos-Gonzalez-Angulo, and J. Yuen-Zhou, Chem. Sci. **9**, 6325 (2018).
[12]J. A. Hutchison, T. Schwartz, C. Genet, E. Devaux, and T. W. Ebbesen, Angew. Chem. Int. Ed. **51**, 1592 (2012).
[13]A. Thomas, L. Lethuillier-Karl, K. Nagarajan, R. M. A. Vergauwe, J. George, T. Chervy, A. Shalabney, E. Devaux, C. Genet, J. Moran, and T. W. Ebbesen, Science **363**, 615 (2019).
[14]A. Mandal, T. D. Krauss, and P. Huo, J. Phys. Chem. B **124**, 6321 (2020).
[15]M. Balasubrahmaniyam, A. Simkhovich, A. Golombek, G. Sandik, G. Ankonina, and T. Schwartz, Nature Materials **22**, 338 (2023).
[16]R. Pandya, A. Ashoka, K. Georgiou, J. Sung, R. Jayaprakash, S. Renken, L. Gai, Z. Shen, A. Rao, and A. J. Musser, Advanced Science **9**, 2105569 (2022).
[17]D. Xu, A. Mandal, J. M. Baxter, S.-W. Cheng, I. Lee, H. Su, S. Liu, D. R. Reichman, and M. Delor, Nature Communications **14**, 3881 (2023).
[18]B. Liu, X. Huang, S. Hou, D. Fan, and S. R. Forrest, Optica **9**, 1029 (2022).
[19]B. Liu, J. Lynch, H. Zhao, B. R. Conran, C. McAleese, D. Jariwala, and S. R. Forrest, ACS nano **17**, 14442 (2023).
[20]B. X. Chng, E. Mondal, and P. Huo, ChemRxiv , 10.26434/chemrxiv (2024).
[21]F. Herrera and F. C. Spano, Physical Review Letters **116**, 238301 (2016).
[22]F. Herrera and F. C. Spano, ACS photonics **5**, 65 (2018).
[23]M. E. Mondal, E. R. Koessler, J. Provazza, A. N. Vamivakas, S. T. Cundiff, T. D. Krauss, and P. Huo, The Journal of Chemical Physics **159** (2023).
[24]E. Mondal, N. Vamivakas, S. Cundiff, T. Krauss, and P. Huo, ChemRxiv , 10.26434/chemrxiv (2024).
[25]Y. Lai, W. Ying, and P. Huo, The Journal of Chemical Physics **161**, 104109 (2024).
[26]L. Qiu, A. Mandal, O. Morshed, M. T. Meidenbauer, W. Girten, P. Huo, A. N. Vamivakas, and T. D. Krauss, The Journal of Physical Chemistry Letters **12**, 5030 (2021).
[27]M. Amin, E. R. Koessler, O. Morshed, F. Awan, N. M. Cogan, R. Collison, W. Girten, C. S. Leiter, A. N. Vamivakas, P. Huo, *et al.*, Chemrxiv (2023).
[28]O. Morshed, M. Amin, N. Cogan, E. R. Koessler, R. Collison, T. M. Tumiel, W. Girten, F. Awan, L. Mathis, P. Huo, *et al.*, The Journal of Chemical Physics **161** (2024).
[29]F. F. Fernandez, N. G. Sinai, M. J. H. Tan, S. M. Park, E. R. Koessler, T. D. Krauss, P. Huo, and T. W. Odom, ACS Nano **18**, 15177 (2024).
[30]W. Ying, M. E. Mondal, and P. Huo, The Journal of Chemical Physics **161**, 064105 (2024).
[31]B. X. Chng, W. Ying, Y. Lai, A. N. Vamivakas, S. T. Cundiff, T. Krauss, and P. Huo, ChemRxiv , 10.26434/chemrxiv (2024).
[32]J. Galego, F. J. Garcia-Vidal, and J. Feist, Physical Review X **5**, 041022 (2015).
[33]R. H. Tichauer, J. Feist, and G. Groenhof, J. Chem. Phys. **154**, 104112 (2021).
[34]D. Sanvitto and S. Kéna-Cohen, Nature materials **15**, 1061 (2016).
[35]A. M. Berghuis, R. H. Tichauer, L. M. de Jong, I. Sokolovskii, P. Bai, M. Ramezani, S. Murai, G. Groenhof, and J. Gómez Rivas, ACS photonics **9**, 2263 (2022).
[36]S. Baieva, O. Hakamaa, G. Groenhof, T. T. Heikkila, and J. J. Toppari, ACS Photonics **4**, 28 (2017).
[37]R. H. Tichauer, D. Morozov, I. Sokolovskii, J. J. Toppari, and G. Groenhof, The Journal of Physical Chemistry Letters **13**, 6259 (2022).
[38]K. B. Arnardottir, A. J. Moilanen, A. Strashko, P. Törmä, and J. Keeling, Physical Review Letters **125**, 233603 (2020).
[39]S. Takahashi and K. Watanabe, The Journal of Physical Chemistry Letters **11**, 1349 (2020).
[40]J. C. Tully, J. Chem. Phys. **137**, 22A301 (2012).
[41]M. Barbatti, Wiley Int. Rev. Comp. Mol. Sci. **1**, 620 (2011).
[42]S. Mai, P. Marquetand, and L. Gonzalez, Int. J. Quantum Chem. **115**, 1215 (2015).
[43]D. Hu, W. Ying, and P. Huo, The Journal of Physical Chemistry Letters **14**, 11208 (2023).
[44]G. Käb, Physical Review E **66**, 046117 (2002).
[45]J. C. Tully, J. Chem. Phys. **93**, 1061 (1990).
[46]S. Hammes-Schiffer and J. C. Tully, J. Chem. Phys. **12**, 4657 (1994).
[47]J. Fregoni, G. Granucci, E. Coccia, M. Persico, and S. Corni, Nat. Commun. **9**, 4688 (2018).
[48]J. Fregoni, S. Corni, M. Persico, and G. Granucci, J. Comput. Chem. **41**, 2033 (2020).
[49]J. Fregoni, G. Granucci, M. Persico, and S. Corni, Chem **6**, 250 (2020).
[50]Y. Zhang, T. Nelson, and S. Tretiak, J. Chem. Phys. **151**, 154109 (2019).
[51]W. Zhou, D. Hu, A. Mandal, and P. Huo, J. Chem. Phys. **157**, 104118 (2022).
[52]D. Hu, A. Mandal, B. M. Weight, and P. Huo, J. Chem. Phys. **157**, 194109 (2022).
[53]D. Hu and P. Huo, J. Chem. Theory Comput. **8**, 2353 (2023).
[54]P. V. Parandekar and J. C. Tully, J. Chem. Theory Comput. **2**, 229 (2006).
[55]J. E. Subotnik, A. Jain, B. Landry, A. Petit, W. Ouyang, and N. Bellonzi, Annu. Rev. Phys. Chem. **67**, 387 (2016).
[56]H. Meyer and W. H. Miller, J. Chem. Phys. **70**, 3214 (1979).
[57]W. H. Miller and S. J. Cotton, Faraday Discuss. **195**, 9 (2016).
[58]P. Huo and D. F. Coker, J. Chem. Phys. **135**, 201101 (2011).
[59]P. Huo and D. F. Coker, Mol. Phys. **110**, 1035 (2012).
[60]S. J. Cotton and W. H. Miller, J. Chem. Phys. **139**, 234112 (2013).
[61]S. J. Cotton and W. H. Miller, J. Phys. Chem. A **117**, 7190 (2013).
[62]C.-Y. Hsieh and R. Kapral, J. Chem. Phys. **137**, 22A507 (2012).

[63]C.-Y. Hsieh and R. Kapral, J. Chem. Phys. **138**, 134110 (2013).
[64]G. Stock and M. Thoss, Phys. Rev. Lett. **78**, 578 (1997).
[65]M. Thoss and G. Stock, Phys. Rev. A **59**, 64 (1999).
[66]J. E. Runeson and J. O. Richardson, J. Comp. Phys. **151**, 044119 (2019).
[67]J. E. Runeson and J. O. Richardson, J. Comp. Phys. **152**, 084110 (2020).
[68]D. Bossion, W. Ying, S. Chowdhury, and P. Huo, J. Chem. Phys. **157**, 084105 (2022).
[69]J. R. Mannouch and J. O. Richardson, The Journal of Chemical Physics **153** (2020).
[70]J. R. Mannouch and J. O. Richardson, The Journal of Chemical Physics **153** (2020).
[71]X. Sun, H. Wang, and W. H. Miller, J. Chem. Phys. **109**, 7064 (1998).
[72]Q. Shi and E. Geva, The Journal of Physical Chemistry A **108**, 6109 (2004).
[73]W. Zhou, A. Mandal, and P. Huo, J. Phys. Chem. Lett. **10**, 7062 (2019).
[74]D. Hu, Y. Xie, J. Peng, and Z. Lan, J. Chem. Theory Comput. **17**, 3267 (2021).
[75]B. M. Weight, A. Mandal, and P. Huo, J. Chem. Phys. **155**, 084106 (2021).
[76]B. Weight, A. Mandal, D. Hu, and P. Huo, ChemRxiv , 10.26434/chemrxiv (2024).
[77]S. N. Chowdhury, A. Mandal, and P. Huo, J. Chem. Phys. **154**, 044109 (2021).
[78]M. A. Saller, A. Kelly, and E. Geva, The Journal of Physical Chemistry Letters **12**, 3163 (2021).
[79]L. Wang, D. Trivedi, and O. V. Prezhdo, J. Chem. Theory Comput. **10**, 3598 (2014).
[80]S. J. Cotton and W. H. Miller, J. Chem. Phys. **150**, 194110 (2019).
[81]D. Bossion, W. Ying, S. Chowdhury, and P. Huo, J. Comp. Phys. **157**, 084105 (2022).
[82]Y. Tanimura and R. Kubo, Journal of the Physical Society of Japan **58**, 101 (1989).
[83]Y. Yan, The Journal of chemical physics **140**, 054105 (2014).
[84]Y. Yan, J. Jin, R.-X. Xu, and X. Zheng, Frontiers of Physics **11**, 1 (2016).
[85]M. A. Zeb, P. G. Kirton, and J. Keeling, ACS Photonics **5**, 249 (2018).
[86]M. Taylor, A. Mandal, and P. Huo, ChemRxiv , 10.26434/chemrxiv (2024).
[87]M. Tavis and F. W. Cummings, Physical Review **170**, 379 (1968).
[88]A. O. Caldeira and A. J. Leggett, Annals of physics **149**, 374 (1983).
[89]A. Nitzan, *Chemical dynamics in condensed phases: relaxation, transfer and reactions in condensed molecular systems* (Oxford university press, 2006).
[90]E. R. Koessler, A. Mandal, and P. Huo, J. Chem. Phys. **157**, 064101 (2022).
[91]T. E. Li, A. Nitzan, and J. E. Subotnik, J. Chem. Phys. **156** (2022), 10.1063/5.0079784.
[92]J. A. Campos-Gonzalez-Angulo and J. Yuen-Zhou, J. Chem. Phys. **156**, 194308 (2022).
[93]U. Müller and G. Stock, J. Chem. Phys. **111**, 77 (1999).
[94]S. J. Cotton and W. H. Miller, J. Chem. Phys. **145**, 144108 (2016).
[95]T. Ozaki, Phys. Rev. B **75**, 035123 (2007).
[96]J. Hu, R.-X. Xu, and Y. Yan, J. Chem. Phys. **133**, 101106 (2010).
[97]J. Hu, M. Luo, F. Jiang, R.-X. Xu, and Y. Yan, J. Chem. Phys. **134**, 244106 (2011).
[98]Q. Shi, L. Chen, G. Nan, R.-X. Xu, and Y. Yan, The Journal of chemical physics **130**, 084105 (2009).
[99]A. Kelly, R. van Zon, J. Schofield, and R. Kapral, J. Chem. Phys. **136**, 084101 (2012).
[100]M. S. Church, T. J. H. Hele, G. S. Ezra, and N. Ananth, J. Chem. Phys. **148**, 102326 (2018).
[101]P. Fowler-Wright, B. W. Lovett, and J. Keeling, Phys. Rev. Lett. **129**, 173001 (2022).
[102]L. P. Lindoy, A. Mandal, and D. R. Reichman, Nanophotonics **13**, 2617 (2024).
[103]J. B. Pérez-Sánchez, A. Koner, N. P. Stern, and J. Yuen-Zhou, Proceedings of the National Academy of Sciences **120**, e2219223120 (2023).
[104]J. B. Pérez-Sánchez, F. Mellini, J. Yuen-Zhou, and N. C. Giebink, Physical Review Research **6**, 013222 (2024).
[105]A. Wu, J. Cerrillo, and J. Cao, Nanophotonics **13**, 2575 (2024).
[106]Y. Liu, E. Mulvihill, and E. Geva, J. Chem. Phys. **161**, 164101 (2024).